Metallicity effects in long gamma-ray burst populations in a ΛCDM Universe

L.A. Bignone[a], L.J. Pellizza[b], P.B. Tissera[a]

[a]*Departamento de Ciencias Físicas, Universidad Andres Bello, Av. Republica 220, Santiago, Chile.*
[b]*Instituto Argentino de Radioastronomía, CIC, CONICET, C.C. 5 (1894) Villa Elisa, Pcia. de Buenos Aires, Argentina*

Abstract

The use of long γ-ray burst as star formation tracers is suspected to be affected by a possible dependence of the production or luminosity of these sources on the metallicity of their stellar progenitors. Selection effects are an alternative explanation. Our aim is to explore the nature of metallicity effects in long γ-ray burst populations using hydrodynamical cosmological simulations that include chemical evolution. We construct long γ-ray burst and host galaxy model populations using galaxy catalogues built from cosmological hydrodynamical simulations, making different assumptions on the nature of metallicity effects. We explore the ability of these models to reproduce an observational dataset that combines redshifts, prompt γ-ray emission observables from *Swift* and *Fermi* satellites, and HG properties from the largely unbiased BAT6 sample. Our results suggest that metallicity effects are more prompted to enhance the production rate of these sources at low metallicities, than to increase the burst luminosities. This is a statistically robust result based on the deviance information criterion. The metallicity threshold of these effects lies in the range $[0.3 - 0.6]Z_\odot$, but can not be constrained more precisely with present data and models. In the self-consistent star formation and metal enrichment scenario presented by our simulation, only models with a metallicity-dependent long γ-ray bust rate are successful at reproducing the γ-ray properties of these sources, their redshift distribution, and the masses and metallicities of their host galaxies, simultaneously. Models with a metallicity-dependent luminosity can reproduce observations, but are not statistically favoured in comparison to a metallicity-dependent production rate. Our simulations also predict that high metallicity hosts are possible even in the presence of a metallicity threshold for long γ-ray burst production. Our results support the view of long γ-ray bursts being produced by the collapse of low-metallicity, massive stars. This strongly suggests that they are biased tracers of the cosmic star formation at lower redshifts.

Keywords:
gamma-ray burst: general, galaxies: star formation, galaxies: abundances

1. Introduction

Long γ-ray bursts (LGRBs) are transient, very luminous ($L \sim 10^{51} \, \mathrm{erg \, s^{-1}}$) high energy sources. Their prompt emission lasts typically some tens of seconds, and is detected at photon energies from keVs to GeVs. It is followed by an afterglow at lower frequencies, from X rays to radio waves, which lasts up to several months. Due to their large luminosities LGRBs can be observed at very high redshifts, and in many cases their host galaxies (HGs) have been identified. Vedrenne & Atteia (2009) present a thorough review on these sources.

Current theoretical models propose that LGRBs occur during the collapse of massive, short-lived stars, due to the accretion of part of the stellar envelope onto the collapsed core (Woosley, 1993; Woosley & Heger, 2006; Yoon et al., 2006). This idea is supported by observations of ongoing star formation (SF) in most HGs (Le Floc'h et al., 2003; Savaglio et al., 2009), and by the association of most LGRBs with core-collapse hypernovae (Hjorth et al., 2003; Della Valle et al., 2006). LGRBs would then be valuable tools for the investigation of the cosmic SF rate (SFR), because they would trace the whole star-forming galaxy population down to low-mass and high-redshift systems, that can not be currently detected with other methods (Wijers et al., 1998).

However, two kinds of results suggest the possible existence of biases in these tracers. The first one is the increase of the ratio between the observed LGRB rate and the SFR with redshift (e.g. Firmani et al., 2004; Daigne et al., 2006; Salvaterra & Chincarini, 2007; Campisi et al., 2010; Wanderman & Piran, 2010). This might be due to selection effects affecting the determination of LGRB redshifts. Salvaterra et al. (2012) claim that they have found the same behaviour in a complete sample of LGRB redshifts. This would indicate an evolution of the number of LGRBs produced per unit of newborn stellar mass (*density evolution*, DE), increasing towards high redshift. On the other hand, as the LGRB samples are flux-limited, an evolution of the luminosity function (LF) of LGRBs (*luminosity evolution*, LE), with the LGRB luminosity being

higher in the past, would also be possible. As stated by Salvaterra et al. (2012), the evidence is yet inconclusive regarding which effect is responsible for the behaviour of the observed LGRB rate. Disentangling the contributions of DE and LE to the observed evolution is important, because they would introduce different biases in the LGRB–SFR relation.

The second result is the distribution of the colours and luminosities of HGs, which are bluer and less luminous than those galaxies that provide most of the cosmic SF at low redshift (Le Floc'h et al., 2003). They are also metal-poor compared to equally-luminous star-forming counterparts in the local Universe (Stanek et al., 2006; Savaglio et al., 2009; Graham & Fruchter, 2013; Jimenez & Piran, 2013). This could be the result of selection effects, as most HGs are detected by the precise positioning of LGRBs given by optical afterglows (Hjorth et al., 2012; Perley et al., 2013; Perley et al., 2016). High-metallicity HGs containing large amounts of dust that obscure afterglows would then be missed by HG searches. Indeed, many dark LGRBs (those with a small ratio of optical to X-ray afterglow luminosities, Jakobsson et al., 2004) have been found, some of them in dusty HGs (e.g., Perley et al., 2009).

Alternatively, LGRB progenitors might indeed be metal-poor stars, as some theoretical models propose (Woosley & Heger, 2006; Yoon et al., 2006). This hypothesis is appealing, because coupled to the cosmic chemical enrichment it would imply a DE. Moreover, if the progenitor metallicity influences also the luminosity of LGRBs, it would imply a LE. In this case, observed HGs would be biased to metal-poor objects because they would produce more luminous LGRBs. The few super-solar-metallicity hosts found recently (Levesque et al., 2010; Savaglio et al., 2012; Perley et al., 2013) are the main challenge to the existence of metallicity effects in LGRBs. They might be the result of an inhomogeneous galaxy composition with low-metallicity regions in an otherwise high-mean-metallicity galaxy. Or, they might be a piece of evidence indicating that former HG samples were heavily biased towards low-metallicity, low-dust-content objects. In any case, the question of the influence of the metallicity of the progenitors on LGRB production or luminosity, if any, is far from being settled.

Some of the previous works devoted to this problem are based on the investigation of the observed LGRB redshift distribution only (Daigne et al., 2006; Salvaterra et al., 2012). Other works explore the observed properties of HGs (Nuza et al., 2007; Chisari et al., 2010; Campisi et al., 2011; Artale et al., 2011; Bignone et al., 2017). usually assuming a fixed LF and taking into account only DE. As both observables probe different aspects of the putative metallicity effects on LGRBs, a step forward could be taken by a simultaneous, self-consistent analysis of both of them. It is the aim of this work to perform such analysis. For this task, we resort to cosmological hydrodynamical simulations of galaxy formation, that provide a self-consistent description of the cosmic SF history and chemical evolution, and therefore constitute a powerful tool to study the relationship between SF and LGRBs. Cosmological hydrodynamical simulations have succeeded in matching the latest data on the SFR (Behroozi et al., 2013), and also in describing the chemical properties of galaxies. Indeed, they have already been used to investigate the properties of LGRB HGs (e.g. Nuza et al., 2007; Artale et al., 2011).

We use galaxy catalogues constructed from the simulations (Pedrosa & Tissera, 2015; Tissera et al., 2016) to model the properties of LGRB populations through Monte Carlo techniques, under different assumptions for the nature of metallicity effects. We compare the predictions of these models with the latest observations obtained by *Swift* and *Fermi* (von Kienlin et al., 2014; Gruber et al., 2014), and with the latest data from the BAT6 HG sample (Salvaterra et al., 2012; Vergani et al., 2015; Japelj et al., 2016). The fact that cosmological hydrodynamical simulations provide the metallicity of the stellar populations in a given galaxy, allows us to explore also the nature of high-metallicity HGs.

This paper is organised as follows. Section 2 provides an overview of the numerical methods used to construct LGRB model populations, and Section 3 presents the results obtained by comparing our model predictions to observations. In section 4 we discuss our findings and presents our conclusions.

2. Numerical model

2.1. Cosmological simulations

We use the cosmic SF and chemical history of a numerical simulation performed with the TreePM/SPH code P-GADGET3 (Springel, 2005), which includes star formation, chemical enrichment, metal-dependent cooling, a multiphase treatment of gas, and supernova (SN) feedback, as described by Scannapieco et al. (2005, 2006). The simulation represents a periodic box of $10h^{-1}$ Mpc comoving side, that evolves up to redshift $z = 0$ according to a Λ-CMD cosmology with parameters $\Omega_\Lambda = 0.7$, $\Omega_m = 0.3$, $\Omega_b = 0.04$, $\sigma_8 = 0.9$, and $H_0 = 100h$ km s^{-1} Mpc^{-1}, with $h = 0.7$. It computes the evolution of 230^3 dark matter particles of mass $5.9 \times 10^6 h^{-1} M_\odot$, and initially 230^3 gas particles of mass $9.1 \times 10^5 h^{-1} M_\odot$. The adopted gravitational softening length is $0.5h^{-1}$ kpc. A more thorough description of this simulation (hereafter referred to as S230D) can be found in Pedrosa & Tissera (2015) and Tissera et al. (2016).

The SN feedback model adopted for this work includes Type II (SNII) and Type Ia (SNIa) supernova events, that distribute energy and metals within the cold and hot phases of the interstellar medium. A detailed description of the SN feedback can be found in Pedrosa & Tissera (2015). This model is successful at driving mass-loaded winds during starbursts, and at regulating the star formation activity during quiescent star formation regimes (Scannapieco et al., 2006).
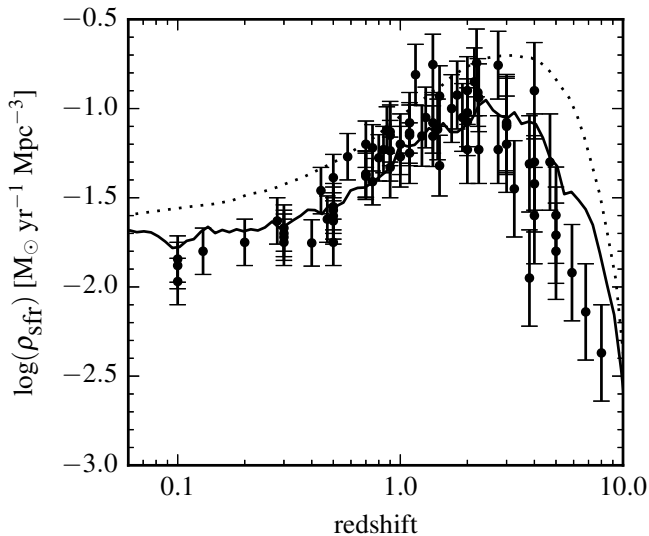
Figure 1: The cosmic star formation rate density for simulations S230D (solid line) and the MS (dotted line). The observations compiled by Behroozi et al. (2013) (circles) are included for comparison.
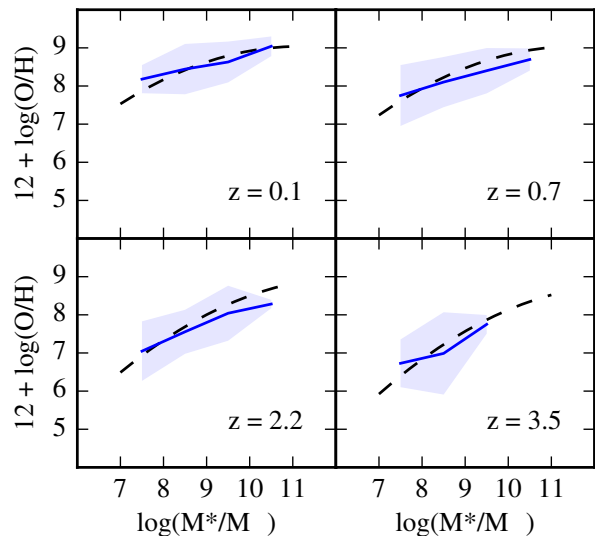

Figure 2: Mass-metallicity relationship for simulated galaxies in S230D (solid lines), for redshifts $z = 0$ (top left), 0.7 (top right), 2.5 (bottom left) and 3.5 (bottom right). Shaded regions represent the 68 percent confidence region. Dashed lines are fits to the observed data from Maiolino et al. (2008). For simulated galaxies, the metallicity is that of their stellar population (see text for details).

Initially, the chemical composition of the gas is assumed to be primordial, with $X_H = 0.76$ and $X_{He} = 0.24$. The SN events distribute 80 percent of the new elements into the cold phase. The chemical model follows the enrichment of 12 isotopes (^{1}H, ^{2}He, ^{12}C, ^{16}O, ^{24}Mg, ^{28}Si, ^{56}Fe, ^{14}N, ^{20}Ne, ^{32}S, ^{40}Ca and ^{62}Zn). The nucleosynthesis models used are those of Iwamoto et al. (1999) and Woosley & Weaver (1995) for SNIa and SNII, respectively. The number of SNII is computed adopting the initial mass function (IMF) of Salpeter, and considering all stars with mass above 8 $M_\odot$ as SNII progenitors. The SNIa rate is estimated using the simple model proposed by Mosconi et al. (2001) (see also Jiménez et al., 2015).

In order to compare our results to previous works, and since our simulated volume is small, we resort to the galaxy catalogue of De Lucia & Blaizot (2007), constructed on the *Millennium Simulation* (hereafter MS, Springel et al., 2005). We apply our LGRB model (described in the next section) to this galaxy catalogue, and test if it behaves similarly and if it provides results consistent with those derived from the hydrodynamical simulation. It is important to note that De Rossi et al. (2013) compared the growth of haloes of different masses as a function of redshift in S230D and the MS, finding consistent trends.

2.2. The cosmic star formation rate

Matching the cosmic star formation rate (cSFR) of numerical simulations to observations remains a difficult task. A growing number of galaxy observations put increasing constraints on galaxy formation models, which require ever more sophisticated models of stellar feedback to account for the build-up of stellar mass in galaxies. The reported cSFR has changed considerably in the last years,

specially at redshifts $z > 3$, as new galaxy observations became available and assumptions about the amount of dust obscuration were revised (Behroozi et al., 2013).

The choice of the cSFR will ultimately determine the intrinsic LGRB rate and redshift distribution, therefore it is important to examine it carefully. In our case, the cSFR is determined by the star formation and SN feedback models of the numerical simulation. Figure 1 shows a comparison of the simulated cSFR with observational results compiled by Behroozi et al. (2013). The simulation closely matches observations up to redshift $z \sim 4$, and exhibits a small excess for higher redshifts. We do not expect this simulation to match closely the observed cSFR but to follow the global trend since the simulated box is small. In order to compare our results to a simulation spanning a larger volume, we applied a similar analysis to the MS catalogues. Figure 1 shows the corresponding cSFR, which presents a slight excess at all redshifts.

The mass metallicity relationship (MZR) of S230D presents the expected slope at all redshifts, but has a lower zero point at low redshift than that reported by Tremonti et al. (2004).[1] Also, the evolution with redshift is weaker than that suggested by observations. We can recover the observed behaviour of the MZR by renormalising the metallicity of the simulation, using the parametrised analytical model of Maiolino et al. (2008), which is set to match Tremonti et al. (2004) data. This procedure assumes that the mean abundances of the gas phase sample adequately

---

[1]Note that there are several papers discussing the calibration of the metallicity estimations (e.g. Kewley & Dopita, 2002).
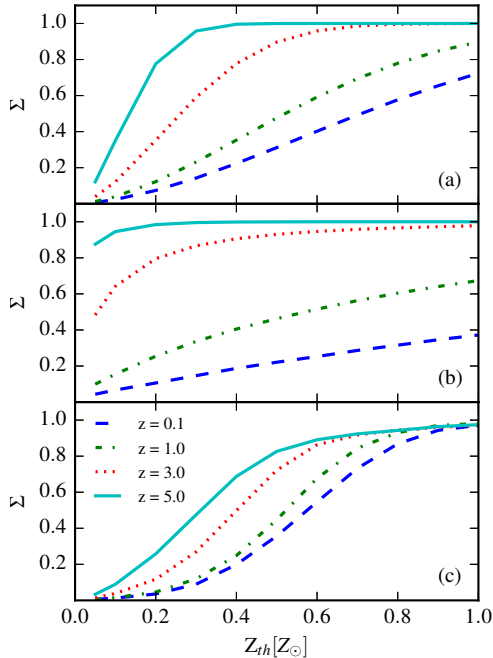
Figure 3: Mass fraction of newborn stars with a metallicity below a given threshold Z_{th}, for (a) the analytical model used by Langer & Norman (2006), (b) S230D, and (c) the MS. The lines correspond to redshift $z = 0.1$ (dashed), 1 (dash-dotted), 3 (dotted), and 5 (solid).

those of star forming regions. Figure 2 shows the MZR of S230D after renormalization, for redshifts 0, 0.7, 2.5, and 3.5. A good agreement with observations is achieved. This renormalized value will only be used to set the abundances of the LGRB progenitor stars.

Given that we want to construct models in which LGRBs are produced only in metal-poor environments, it is worthwhile to examine the fraction $\Sigma(z, Z_{\mathrm{th}})$ of the newborn stellar mass with metallicities below a certain threshold Z_{th}, at a given redshift z. An analytical prescription for Σ has been previously used to study the metallicity dependence of LGRBs progenitors (Langer & Norman, 2006; Salvaterra et al., 2012). For S230D and the MS, Σ can be computed directly from the simulation. However, a key difference between both simulations is that, while for S230D (a hydrodynamical simulation) we can trace gas and stellar populations locally, we can only work with global properties of galaxies in the MS, given that the galactic catalogue was built from a semianalytical model. Therefore, when computing $\Sigma(z, Z_{\mathrm{th}})$ we consider the mass and metallicity of individual star forming gas particles in the case of S230D, while only the average metallicity and star formation of galaxies in the case of the MS.

It is also worthwhile to point out, that given that LGRBs progenitors are massive, short lived stars, their metallicity is expected to closely match that of star forming regions. Therefore, progenitor metallicies are well represented by

gas phase metallicities in this case.

Figure 3 shows that in all cases the chemical enrichment grows with decreasing redshift, describing the cosmic chemical history. This behaviour determines that of the LGRB intrinsic rate. If LGRBs were only produced below a certain metallicity threshold, all models would predict that the peak of the LGRB rate should shift to higher redshift when the threshold decreases. The magnitude of the shift depends on the detailed evolution of $\Sigma(z, Z_{\mathrm{th}})$ with Z_{th} and z, and therefore differs from one model to another.

The large differences between S230D and MS can be attributed to the fact that the detailed chemical evolution of galaxies in hydrodynamical simulations depend on interconected factors such as star formation, feedback processes and inflows and outflows of material between the galaxy and the intergalactic medium. Some of these processes cannot be resolved accurately with current resolution and are therfore included as subgrid models which have large effects on the detailed local metallicity properties of simulated galaxies. Also it should be point out the different technical nature of the MS and S230D, which in practice means that the metallicities being consided are slighly different in both cases, as mentioned above.

2.3. Models for LGRB populations

Because of the relationship between LGRBs and massive stars, we first consider a scenario in which LGRBs are produced only by stars above a certain minimum mass M_{min}, and with a negligible lifetime compared to the evolution time-scale of a galaxy. In this case, LGRBs are unbiased tracers of star formation (there are no metallicity effects and therefore no evolution of LGRB populations) and consequently, the LGRB rate density is related to the cSFR density according to

$$\Psi_{\mathrm{LGRB}}(z) = \frac{\int_{M_{\mathrm{min}}}^{100\,M_\odot} \psi(m)dm}{\int_{0.1\,M_\odot}^{100\,M_\odot} m\psi(m)dm} \dot{\rho}_{\mathrm{SFR}}(z), \qquad (1)$$

where ψ is the Salpeter (1955) initial mass function with lower and upper stellar mass limits of $0.1\,M_\odot$ and $100\,M_\odot$, respectively. This is our base scenario, to which those including metallicity effects will be compared.

A preference of LGRBs for low-metallicity environments can be included in the model by convolving the cosmic chemical enrichment Σ with Eq. 1, to yield the evolution of the cosmic LGRB rate density. This results in an LGRB redshift distribution skewed from the unbiased rate,

$$\Psi_{\mathrm{LGRB}}(z, Z_{\mathrm{th}}) = \Sigma(z, Z_{\mathrm{th}})\Psi_{\mathrm{LGRB}}(z). \qquad (2)$$

This approach adopts a simple threshold in the production of LGRBs at a given metallicity Z_{th}. We construct four different DE scenarios, adopting $Z_{\mathrm{th}} = 0.1,\ 0.3,\ 0.6\ Z_\odot$.

In order to compare the predictions of each scenario with observations, we generate a population of LGRBs according to the model described above. For each LGRB, its

redshift is drawn from the distribution $\Psi_{\mathrm{LGRB}}(z, Z_{\mathrm{th}})$, and its fundamental intrinsic properties, the isotropic peak luminosity L and the spectral peak energy E_{p}, are assigned as follows. The former is sampled from a predefined LF (f_L), for which we have adopted a lognormal distribution with mean $\mu_L = \langle \log(L/1 \text{ erg s}^{-1}) \rangle$ and standard deviation $\sigma_{\log L}$ taken as free parameters.

Many forms for the LGRB luminosity function have been considereded, for example Schechter functions, truncated power laws, broken power-laws and lognormal functions. In this case we have chosen a lognormal distribution because our main objetive in this work is not to provide a detailed description of the luminosity function, but instead to compare the merits of the DE and LE scenarios in explaining the metallicity dependence of LGRBs. A lognormal distribution has the smallest number of free paramenters possible and can therefore provide a more meaningful statiscal comparison between scenarios. Lognormal luminosity functions for LGRBs have been considered in previous works such as Elliott et al. (2012); Belczynski et al. (2010).

The adopted model for the spectrum is a Band function $B(E)$ (Band et al., 1993), with fixed typical values for the low- and high-energy indices ($\alpha = -1$, $\beta = -2.25$ Kaneko et al., 2006; Nava et al., 2008). We assume the existence of a correlation between E_{p} and L (Yonetoku et al., 2004), given by

$$E_{\mathrm{p}} = 380 \,\mathrm{keV} \left(\frac{L}{1.6 \times 10^{52} \,\mathrm{erg}\,\mathrm{s}^{-1}} \right)^{0.43}. \quad (3)$$

We further account for the observed scatter in this correlation by drawing the actual E_{p} value for each LGRB from a lognormal distribution with mean given by equation 3, and dispersion $\sigma_{E_{\mathrm{p}}}$ taken as a free parameter of our model (cf. Daigne et al., 2006).

Once the redshift, luminosity and spectrum of each LGRB are known, the peak photon flux observed by a satellite with an observational window in the energy range $[E_{\mathrm{min}}, E_{\mathrm{max}}]$ can be computed as

$$P = \frac{(1+z)}{4\pi d_{\mathrm{L}}^2(z)} \int_{(1+z)E_{\mathrm{min}}}^{(1+z)E_{\mathrm{max}}} B(E) dE, \quad (4)$$

where $d_{\mathrm{L}}(z)$ is the luminosity distance and $B(E)$ is the burst spectrum in the rest frame of the source normalized to the isotropic peak luminosity by imposing the condition $L = \int_{1\mathrm{keV}}^{10^4\mathrm{keV}} E B(E) dE$. The observed LGRB rate can then be calculated as

$$R_{\mathrm{LGRB}} = f_{\mathrm{jet}} \int_0^{z_{\mathrm{max}}} \int_{L_{\mathrm{min}}}^{\infty} \frac{\Psi_{\mathrm{LGRB}}(z, Z_{\mathrm{th}})}{1+z} \frac{dV}{dz} \epsilon(P) f_L(L) \, dL \, dz, \quad (5)$$

where $2\pi f_{\mathrm{jet}}$ is the solid angle subtended by the LGRB jet, dV/dz is the redshift-dependent volume element, and the factor $(1+z)$ accounts for time dilation. The factor $\epsilon(P)$ accounts for the sky coverage and efficiency of the detector

and Lmin is the minimum luminosity required by a burst at redshift z to produce a peak flux of P_{min}, the peak flux limit of the survey being considered.

Following previous works (e.g. Chisari et al., 2010)) we assume throughout this work a value $f_{\mathrm{jet}} = 10^{-3}$, which is close to the observed average estimations (Ghirlanda et al., 2007).

The differential peak flux distribution can be determined by the observed rate of bursts with peak flux between P_1 and P_2 (i.e. Salvaterra & Chincarini, 2007; Salvaterra et al., 2009; Howell et al., 2014, and references therein) as

$$\frac{dN}{dt}(P_1 < P < P_2) = f_{\mathrm{jet}} \int_0^{z_{\mathrm{max}}} dz \frac{\Psi_{\mathrm{LGRB}}(z, Z_{\mathrm{th}})}{1+z} \frac{dV}{dz}$$
$$\times \int_{L(P_1,z)}^{L(P_2,z)} \epsilon(P) f_L(L) \, dL, \quad (6)$$

Apart from the scenarios that describe the metallicity-driven LGRB DE, we explore others in which a metallicity-dependent LGRB LF produces a LE. In these scenarios, the LGRB rate follows the SFR in an unbiased way according to equation 1, but LGRBs with $Z > Z_{\mathrm{th}}$ have a different LF than the rest. For the sake of simplicity, we adopt the same lognormal shape for both LFs, but with independent parameters which will be fixed by confronting model predictions with observations. Eq. 5 is modified in this case to take into account both LFs, and the whole cosmic SFR density. We adopt three different LE scenarios with $Z_{\mathrm{th}} = 0.1$, 0.3, 0.6 $Z_{\odot}$.

2.4. Determination of the free parameters

In order to contrast the predictions of our model with observations, we use five observables from the LGRB samples detected by *Swift* and *Fermi*:

1. The observed differential peak-flux number counts of bright ($P \geq 1.0$ ph cm^{-2} s^{-1} at the 15–150 keV band) LGRBs, constructed from the *Swift* online catalogue[2] (as of July 2014).
2. The observed spectral peak energy distribution of 218 *Swift* LGRBs (Butler et al., 2007).
3. The observed redshift distribution of the 95-percent complete sample of LGRBs with $P \geq 2.6$ ph cm^{-2} s^{-1}, compiled by Salvaterra et al. (2012, BAT6).
4. The observed differential peak-flux number counts of 764 *Fermi* LGRBs with $P \geq 1.0$ ph cm^{-2} s^{-1} in the 50–300 keV band, constructed from the GBM online Burst Catalogue (von Kienlin et al., 2014).
5. The observed spectral peak energy distribution of 522 *Fermi* bursts from the catalogue of Gruber et al. (2014).

---

[2]http://swift.gsfc.nasa.gov/archive/grb_table/

Two important selection effects are considered in this work when comparing to observations. First, is the detector triggering efficiency. We assume for Swift a triggering efficiency given by a Heaviside step function with threshold at 1.0 ph cm^{-2} s^{-1}, which is consitent with the value determined by Band (2003). For Fermi we assume a triggering efficiency equal to that of BATSE (Stern et al., 2001), however, we point out that the peak flux limit of our sample is greater than the value for which threshold effects become dominant (Paciesas et al., 2012).

Secondly, we have specially chosen to contrast our results regarding the redshift distribution of LGRBs with the 95-percent complete sample of Salvaterra et al. (2012). It has been shown that bright LGRB samples, such as the one used here, are largely unaffected by redshift selection effects (Tan & Wang, 2015). This high level of redshift completeness allows us to constrain our model parameters in an unbiased way.

We optimise the values of the free parameters (LGRB LF parameters, minimum progenitor mass, and dispersion of the Yonetoku et al. 2004 correlation) by jointly fitting the five aforementioned observables. Care is taken to apply to the model LGRB population, the same constrains on peak flux that define the observed samples. Given the large dimensionality of the parameter space, the data fitting is performed via a Markov-Chain Monte Carlo (MCMC) algorithm, because it provides a quick exploration of the important parameter-space regions.

2.5. Host galaxies

With the free parameters already fixed to fit the high-energy observables, we compute the properties of the HG population predicted by each scenario. Following Chisari et al. (2010), we assume that the probability p_{HG} of observing a particular galaxy as a HG is proportional to its contribution to the observed LGRB rate. For DE scenarios,

$$p_{\mathrm{HG}} = \frac{f_{\mathrm{jet}} \dot{M}_*(Z_{\mathrm{th}})}{1+z} \int_0^\infty \epsilon(P) f_L(L) \, dL, \qquad (7)$$

where $\dot{M}_*(Z_{\mathrm{th}})$, the fraction of the SFR of the galaxy that occurs below Z_{th}, is computed from the simulations. For LE scenarios, Eq. 7 must be modified to account for the whole SFR and both LFs. To compute the distributions of the HG properties predicted by our scenarios, we weight the properties of the galaxies in the galaxy catalogue of the S230D simulation by p_{HG}. These predictions are compared to the HGs of the BAT6 sample (Vergani et al., 2015; Japelj et al., 2016) which was constructed on the basis of the brightness of the bursts, on favourable observing conditions (Salvaterra et al., 2012) and independent of the detection of the optical afterglow. Compared to previous studies, these criteria results in a largely unbiased sample. The BAT6 sample is 95 per cent complete in redshift and offers a uniform selection of HGs regardless of galaxies fluxes and colors. We focus our comparison on the z < 1

Table 1: Best-fit parameter values for base (first line) and DE scenarios (lines 2–4).

Z_{th}	$M_{\mathrm{min}} \, [M_\odot]$	μ_L	$\sigma_{\log L}$	σ_{E_p}
—	95	51.1 ± 0.4	0.86 ± 0.07	0.34 ± 0.2
$0.6 Z_\odot$	81	49.8 ± 0.5	1.26 ± 0.08	0.32 ± 0.2
$0.3 Z_\odot$	39	48.2 ± 0.3	1.58 ± 0.08	0.30 ± 0.2
$0.1 Z_\odot$	35	48.5 ± 0.4	1.47 ± 0.08	0.33 ± 0.2

subsample for which Vergani et al. (2015) obtained stellar masses and Japelj et al. (2016) derived star formation rates and metallicities.

3. Results

3.1. Density-evolution scenarios

We compare here the results for DE scenarios with those for the base scenario with no metallicity effects. In all cases we find a good agreement between both Swift and Fermi data, and model predictions for the observed differential peak-flux number counts and spectral peak energy distributions. This is true for both S230D and the MS. We find no statistically significant difference between the predictions of the base scenario and those with different metallicity thresholds. Figure 4 shows the extreme cases of best and worst-fitting models. Other models give very similar results; we do not show them for clarity.

Best-fit parameters are shown in Table 1. As expected, the minimum progenitor mass decreases when Z_{th} decreases. The values of M_{min} are just indicative, as they depend on the adopted value of f_{jet}. Also, the dispersion of the LF becomes larger and its mean decreases with decreasing metallicity threshold. Given that low-luminosity bursts are observable only at short distances (hence in a small cosmic volume), this behaviour effectively implies that the observable part of the LF becomes more skewed, increasing the fraction of high-luminosity bursts among those detected. As we will show later in this section, this is consistent with the fact that a larger fraction of LGRBs is produced at higher redshift when Z_{th} decreases. The dispersion of the Yonetoku et al. (2004) correlation is the same in all scenarios, and agrees with that found by previous works.

Nevertheless, clear differences are detected between the predictions of models with different metallicity thresholds for the observed redshift distribution. Figure 5 shows that the peak of this distribution lies at higher redshift when Z_{th} decreases, which is consistent with the cosmic chemical evolution. This result also implies that the LF must contain a larger fraction of high-luminosity bursts. For S230D, the best fit value of Z_{th} is $0.3 Z_\odot$, while for the MS it increases to $0.6 M_\odot$. This shows that Z_{th} is strongly dependent on the details of the cosmic chemical enrichment. Despite this fact, the existence of a metallicity threshold is a robust result, as the base scenario with no metallicity effects is strongly disfavoured by observations, both in S230D and the MS.
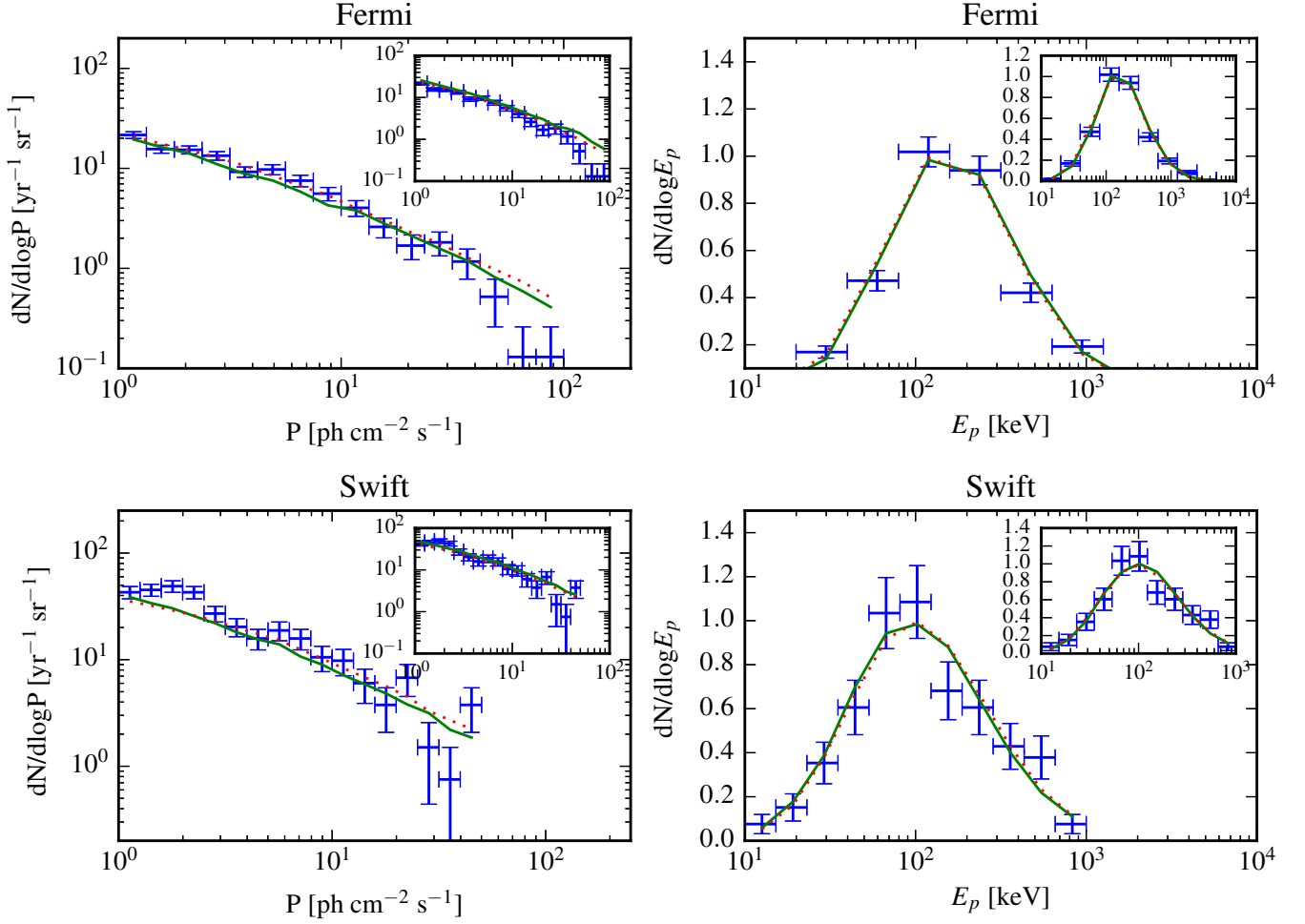
Figure 4: DE scenarios: observed differential peak-flux number counts (left) and spectral peak energy distributions (right). The top row shows *Fermi* data, whereas the bottom row presents *Swift* observations. The predictions of the best S230D DE scenario ($Z_{\text{th}} = 0.3Z_\odot$, solid line) and the worst one (the base scenario, dotted line), are also shown. Vertical error bars represent Poisson uncertainties, whereas horizontal error bars represent the bin sizes. All other values of Z_{th} give similar results, and are not included for clarity. Insets show the corresponding results for the MS; in this case the best fit corresponds to $Z_{\text{th}} = 0.6Z_\odot$.
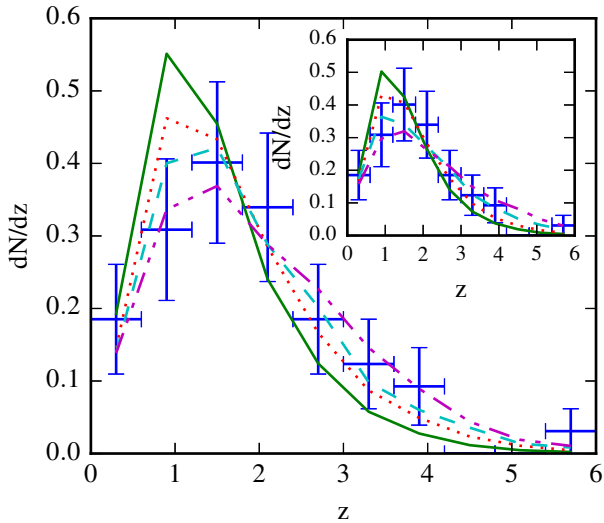
Figure 5: DE scenarios: Observed *Swift* redshift distribution (Salvaterra et al., 2012), together with the predictions of the base scenario (solid line), and DE scenarios with $0.6Z_\odot$ (dotted line), $0.3Z_\odot$ (dashed line) and $0.1Z_\odot$ (dash-dotted line). The inset shows the corresponding plot for the MS.

3.2. Luminosity-evolution scenarios

In order to test the existence of metallicity effects in the LGRB LF, we use the LE scenarios to fit the observational data. The results are very similar to those obtained in the previous section. In all cases we find a good agreement between data and model predictions for the observed differential peak-flux number counts and spectral peak energy distributions. We find no statistically significant difference between the predictions of scenarios with different metallicity thresholds, neither for S230D nor for the MS (Fig. 6).

Interestingly, we find that the greatest difference between the predictions of scenarios with different Z_{th} occurs again for the observed redshift distribution (Fig. 7). Best-fit parameters are shown in Table 2. In order to fit the data, LE scenarios produce a larger fraction of high-luminosity, low-metallicity bursts, observable up to high redshifts. Simultaneously, the mean luminosity of high-metallicity LGRBs is significantly reduced, which causes them only to be observable up to short distances. The best fist model corresponds to $Z_{th} = 0.3Z_\odot$ for S230D, and to $Z_{th} = 0.6Z_\odot$ for the MS.

This result shows that LGRBs originating from low metallicity progenitors are on average significantly more luminous than those from high metallicity progenitors, which is in general agreement with results postulating that LGRBs were more luminous in the past (i.e. Salvaterra et al., 2009), since higher redshift progenitors are expected to have lower metallicities.

3.3. Metallicity of host galaxies

Fig. 8 shows the distribution of the observed HGs in the mass-metallicity (MZ) plane, together with the joint MZ distribution of the HGs in the S230D simulation, for the base and DE scenarios. Observed HGs follow the general MZR of galaxies, which is also the high-probability region in all scenarios. The main differences between the scenarios are seen, as expected, at high metallicities ($Z \gtrsim Z_\odot$). On the one hand, the base scenario predicts a sizeable probability of finding supersolar HGs with low masses ($\log(M_*/M_\odot) \lesssim 9$), whereas in DE scenarios this probability is almost negligible. The latter case is consistent with observations. On the other hand, in all scenarios, HGs with $\log(M_*/M_\odot) > 9.5$ cumulate a large fraction (over 50% in some cases) of the probability, whereas most observed HGs have $\log(M_*/M_\odot) < 9.5$.

To further investigate this issue, in Fig. 9 we show the cumulative metallicity distribution of simulated HGs at different redshifts. Two trends are clearly visible: the fraction of high-metallicity HGs decreases with increasing redshift and with decreasing Z_{th}. The first one is a consequence of the cosmic chemical evolution; the second one can be used to explore metallicity effects, as soon as large HG samples at different redshifts are available. The BAT6 sample of (Japelj et al., 2016) has a mean redshift $\langle z \rangle \simeq 0.7$, therefore we compare them to HGs computed for the closest snapshot of S230D, which corresponds to $z = 0.65$ (dashed line in Fig. 9). The fraction of observed supersolar HGs in the (Japelj et al., 2016) sample is 16(-8 +16)%, accounting for errors, lower than those predicted by the base scenario by a factor of three. DE scenarios provide a closer prediction, but still a factor of two higher than the observed value. These results still favour the existence of metallicity effects over a scenario with no evolution. The failure of our scenarios to reproduce the observed data may indicate the need for a more complex model for metallicity effects, or that some bias still remains in the HG sample. Regarding the last point, we notice that our supersolar metallicity hosts follow the MZ relationship regardless of metallicity threshold, resulting in more massive galaxies at higher metallicity. Dai (2009) found a clear deficit of dark LGRBs, which tend to have more massive HGs, at high peak flux levels. Also Buchner et al. (2016) analysed the X-ray afterglow of Swift LGRBs and found a correlation between HG stellar mass and X-ray obscuration. This implies that the 2.6 ph cm^{-2} s^{-1} flux threshold of the BAT6 sample might be missing some of the more massive hosts. Finally, Graham et al. (2015) studied in detail the HGs with high metallicity in the Graham & Fruchter (2013) sample, which we also show in Fig. 9. These hosts are located in the redshift range covered by the BAT6 sample but are significantly more massive and occupy the same region of the MZ plane predicted to be populated by high metallicity hosts in our simulation.

Regarding HGs, LE scenarios reproduce the same trends found in DE scenarios. Figs. 10 and 11 show the joint MZ

$Z_{\rm th}$	$M_{\rm min}\ [M_\odot]$	$\mu_L^{Z>Z_{\rm th}}$	$\sigma_{\log L}^{Z>Z_{\rm th}}$	$\mu_L^{Z\leq Z_{\rm th}}$	$\sigma_{\log L}^{Z\leq Z_{\rm th}}$	$\sigma_{E_{\rm p}}$
—	95	—	—	51.1 ± 0.3	0.9 ± 0.3	0.34 ± 0.02
$0.6Z_\odot$	96	44.3 ± 0.7	2.32 ± 0.08	51.4 ± 0.5	1.2 ± 0.3	0.33 ± 0.02
$0.3Z_\odot$	81	44.5 ± 0.7	3.44 ± 0.07	50.2 ± 0.4	1.2 ± 0.4	0.32 ± 0.02
$0.1Z_\odot$	53	44.4 ± 0.8	0.64 ± 0.08	49.3 ± 0.4	1.4 ± 0.2	0.35 ± 0.02
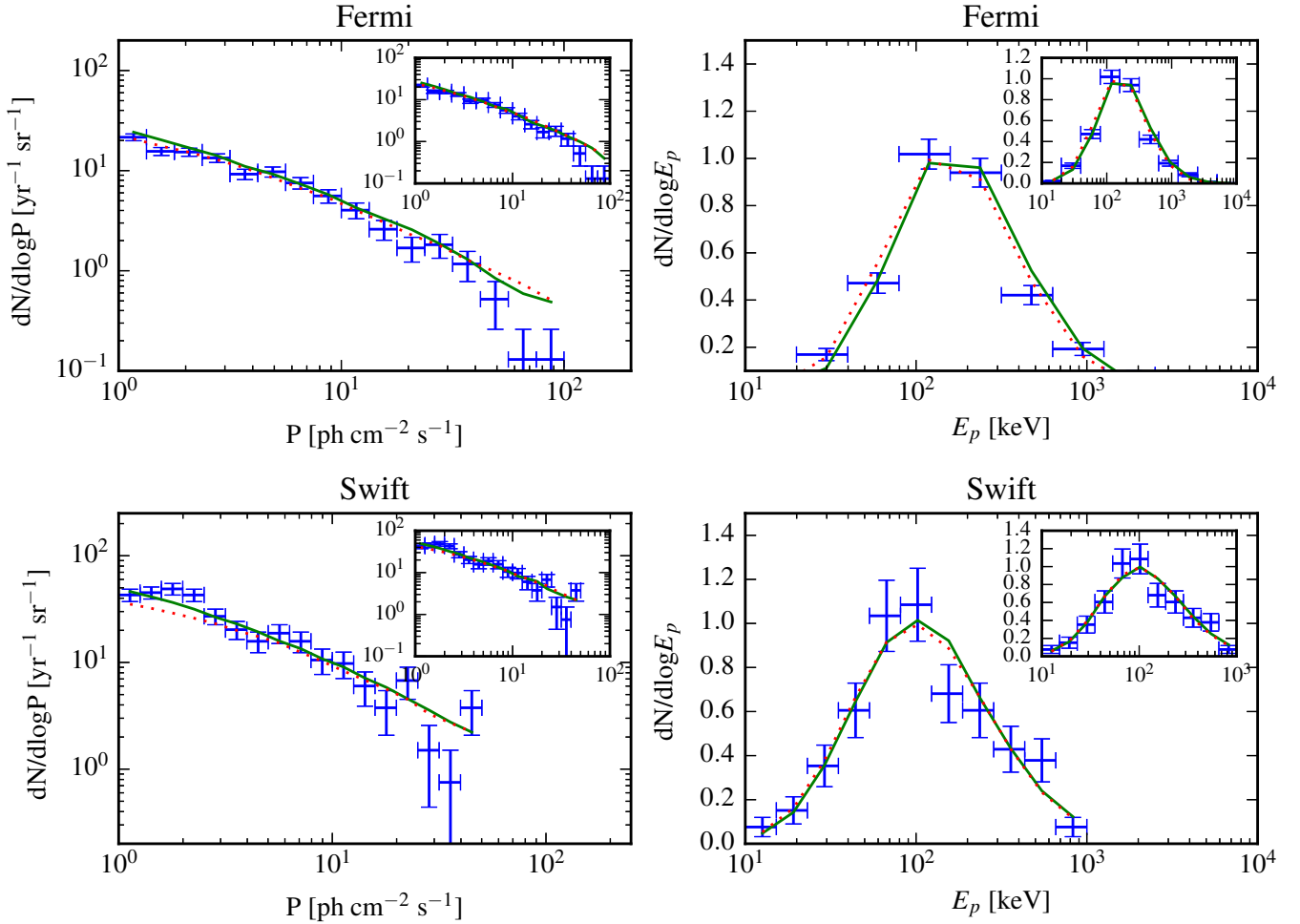
Figure 6: LE scenarios: observed differential peak-flux number counts (left) and spectral peak energy distributions (right). The top row shows *Fermi* data, whereas the bottom row presents *Swift* observations. The predictions of the best S230D LE scenario ($Z_{\rm th} = 0.3Z_\odot$, solid line) and the worst one (the base scenario, dotted line), are also shown. Vertical error bars represent Poisson uncertainties, whereas horizontal error bars represent the bin sizes. All other values of $Z_{\rm th}$ give similar results, and are not included for clarity. Insets show the corresponding results for the MS; in this case the best fit corresponds to $Z_{\rm th} = 0.6Z_\odot$.
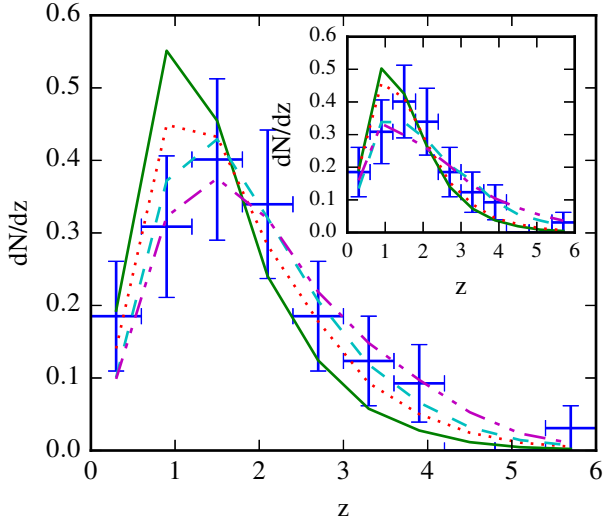
Figure 7: LE scenarios: observed *Swift* redshift distribution (Salvaterra et al., 2012), together with the predictions of the base scenario (solid line), and LE scenarios with $0.6Z_\odot$ (dotted line), $0.3Z_\odot$ (dashed line) and $0.1Z_\odot$ (dash-dotted line). The inset shows the corresponding plot for the MS.
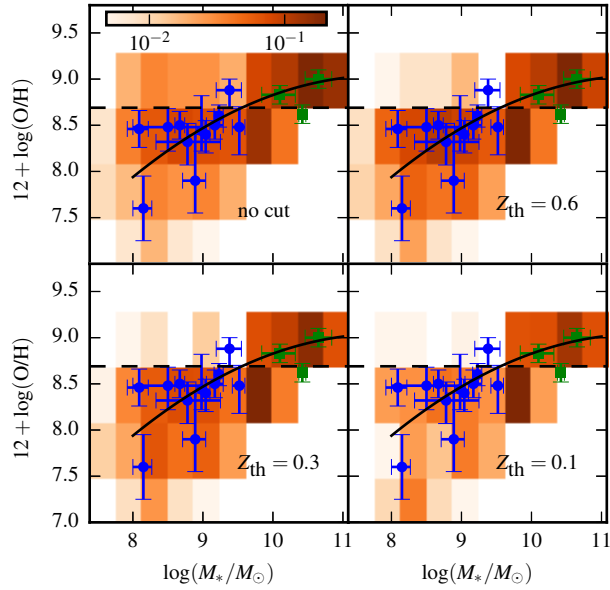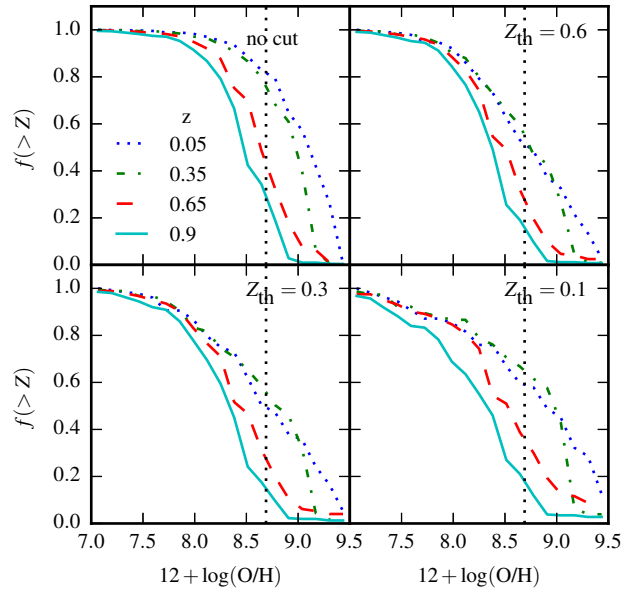

Figure 9: DE scenarios: cumulative metallicity distribution of HGs at $z = 0.05$ in the S230D simulation (dotted blue line), 0.35 (green dash-dotted line), 0.65 (red dashed line), and 0.9 (cyan solid line). The predictions are given for the base scenario (upper left panel), and DE scenarios with $Z_{th} = 0.6Z_\odot$ (upper right panel), $0.3Z_\odot$ (lower left panel) and $0.1Z_\odot$ (lower right panel). The vertical dotted black line represents the solar metallicity. Cf. Fig. 3 of Bignone et al. (2017), where a similar analysis is presented for the Illustris simulation

Figure 8: DE scenarios: joint mass-metallicity distribution of HGs in the S230D simulation. The predicted probability that a HG is observed in each region of the MZ plane is given by the colour of the shade, for the base scenario (upper left panel) and DE scenarios with $Z_{th} = 0.6Z_\odot$ (upper right panel), $0.3Z_\odot$ (lower left panel) and $0.1Z_\odot$ (lower right panel). The BAT6 HG observations from Japelj et al. (2016) (blue circles) and supersolar metallicity HGs from Graham et al. (2015) (green squares) are also plotted, together with the standard galaxy MZR (solid line), and the value of the solar metallicity (dashed line). Cf. Fig. 2 of Bignone et al. (2017), where a similar analysis is presented for the Illustris simulation
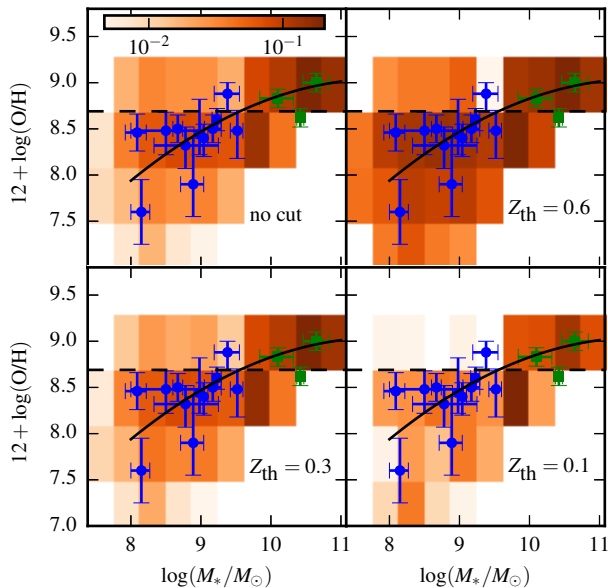
10

Figure 10: LE scenarios: joint mass-metallicity distribution of HGs in the S230D simulation. The predicted probability that a HG is observed in each region of the MZ plane is given by the colour of the shade, for the base scenario (upper left panel) and LE scenarios with $Z_{th} = 0.6Z_{\odot}$ (upper right panel), $0.3Z_{\odot}$ (lower left panel) and $0.1Z_{\odot}$ (lower right panel). The BAT6 HG observations from Japelj et al. (2016) (blue circles) and supersolar metallicity HGs from Graham et al. (2015) (green squares) are also plotted, together with the standard galaxy MZR (solid line), and the value of the solar metallicity (dashed line).
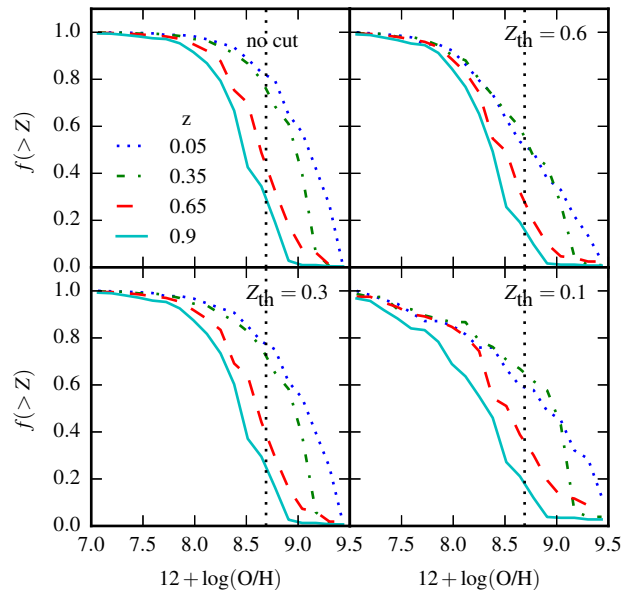
Figure 11: LE scenarios: cumulative metallicity distribution of HGs in the S230D simulation at $z = 0.05$ (dotted blue line), 0.35 (green dash-dotted line), 0.65 (red dashed line), and 0.9 (cyan solid line). The predictions are given for the base scenario (upper left panel), and LE scenarios with $Z_{th} = 0.6Z_{\odot}$ (upper right panel), $0.3Z_{\odot}$ (lower left panel) and $0.1Z_{\odot}$ (lower right panel). The vertical dotted black line represents the solar metallicity (dashed line).

distribution of HGs and their cumulative metallicity distribution for different redshifts, respectively. These are similar to their DE counterparts (Figs. 8 and 9, respectively). The major difference is that LE scenarios predict a significant probability of finding supersolar HGs with low masses ($\log(M_*/M_{\odot}) \lesssim 9$). This behaviour, which is at odds with observations, is similar to that of the base scenario. Therefore, the analysis of HGs provides an extra argument against metallicity effects in the LGRB LF being the explanation of the observed evolution of LGRB populations.

3.4. Comparison of DE and LE scenarios

Comparing DE with LE models, we find that both of them are able to reproduce the observations. There are no readily discernible differences which allow us to choose one over the other. Therefore, we apply a statistical analysis based on the Deviance Information Criterion (DIC, Liddle, 2007) in order to compare the relative merits of both models. The DIC statistic D is easily computed for each scenario from the MCMC runs, and its value decreases for those that better fit the data, therefore taking into account the goodness of the fit. At the same time, it penalizes models with high number of parameters that do not contribute significantly to the goodness of fit, providing an

effective and quantitative implementation of the Occam's razor. As a general rule, scenarios with low values of the DIC statistic should be preferred. Given a set of competing scenarios, the probability of each one is proportional to $\exp(-D/2)$.

Table 3 shows the relative probabilities of our scenarios, with respect to the most probable one in S230D and the MS. The base scenario with no metallicity effects, has a probability six orders of magnitude lower than the best scenario, strengthening our previous result on the existence of metallicity effects. In both simulations, the best DE scenario is preferred over the best LE scenario. The former is sixteen times more probable than the latter in S230D, and six times in the MS. We conclude from our statistical analysis that the model with a metallicity-dependent LF is not able to provide a significantly better fit to the data that justifies its increased complexity. The DE model should then be preferred. This is another robust result of our analysis, which is held by both S230D (a hydrodynamical simulation) and the MS (an N-body simulation plus a semianalytical model). We note that for DE scenarios in the MS, the best-fit Z_{th} value obtained from the DIC ($0.3Z_{\odot}$) differs from that of our previous MCMC analysis ($0.6Z_{\odot}$). This is due to the different statistics used by both methods, and to the fact that these two models provide fits of similar quality to the data (their probabilities are indeed of the same order of magnitude). This fact

11

Table 3: DIC model probabilities, relative to the most probable model of each simulation. The results for the base, DE, and LE scenarios, are tabulated for S230D and the MS.

Scenario	Z_{th}	DIC relative probability	
		S230D	MS
Base	—	5.9×10^{-6}	0.019
DE	$0.6\,Z_\odot$	0.047	0.3
DE	$0.3\,Z_\odot$	1.0	1.0
DE	$0.1\,Z_\odot$	0.066	0.055
LE	$0.6\,Z_\odot$	0.0028	0.16
LE	$0.3\,Z_\odot$	0.06	0.13
LE	$0.1\,Z_\odot$	0.011	0.06

does not change our conclusions.

A more sophisticated model to consider could be one where metallicity affects the luminosity and formation of LGRBs simultaneously. However, our results cautions us from using a more complicated model with the methodology employed in this work. Rate evolution alone appears enough to explain observations, luminosity evolution does not provide a significantly better description of the data and both effects would be hard to disentangle if included simultaneously, which means that extra care should be taken if free parameters are included in the model that would result in degenerate results. Similar considerations are valid if metallicity effects are included on other physical aspects of LGRBs, for example on the jet opening angles.

Another aspect to consider can be a non universal IMF that depends on local environmental factors, such as metallicity. If the IMF changes with local properties, producing more massive stars and thus more potential LGRB progenitors under certain conditions, this can in turn affect the redshift distribution of LGRBs and the properties of their host galaxies. However, a more thorough analysis of the IMF is beyond the scope of this work, since the underlaying simulations were computing using a fixed IMF.

4. Conclusions

We have explored the problem of the metallicity dependence of LGRB populations, using cosmological hydrodinamical simulations of galaxy formation and evolution. We developed different models for LGRB production within these simulations, and tested their predictions against observations of LGRB redshifts, prompt γ-ray emission properties (peak flux and spectral peak energy, measured by *Swift* and *Fermi* observatories), and HGs. The main contribution of our work is twofold: the joint analysis of the LGRBs to hydrodynamical simulations and a semi-analytic model, to assess the robustness of metallicity effects, and the combination of the latest γ-ray data with redshift measures and HG properties to contrast our models.

We found that peak flux and spectral peak energy distributions do not provide by themselves any useful information on the metallicity dependence of LGRBs, but

serve instead as constraints for their LF and the intrinsic spectral properties. The most stringent constraint on possible metallicity effects comes from the redshift distribution and the HG MZR relation, from which we discard the hypothesis that there is no metallicity effect. This result is statically robust, coming out from our hydrodynamical simulation, and a semi-analytic model of the MS, which use different physical models and were run with different numerical approaches. The result does not depend on the nature assumed for the metallicity effects (i.e., changes in the LGRB rate density or in its LF). It also agrees with previous results that use analytical prescriptions for the SFR and the evolution of the metallicity of newborn stars (Daigne et al., 2006; Salvaterra & Chincarini, 2007; Wanderman & Piran, 2010; Campisi et al., 2010; Salvaterra et al., 2012). Therefore, our findings strongly suggest that LGRBs are biased tracers of the cosmic star formation rate in agreement with previous claims.

Assuming a sharp metallicity threshold, our results yields a critical value in the range $Z = [0.3-0.6]Z_\odot$. However, a more precise constraint is not possible to be drawn because of the large errors in the redshift distribution observed by *Swift*, and of the MZR of HGs, and lack of a more precise knowledge of the cosmic chemical evolution, and hence of the distribution of the metallicity of the newborn stars as a function of redshift, among others.

Obtaining more and better observations, and assessing their biases, is a crucial step to solve this problem and to better constrain the evolution of the bias in the determination of the cosmic star formation rate . A redshift distribution obtained with *Fermi* would be also relevant, because its different energy band provide a different window at the redshift- luminosity-spectrum space. Although some redshift measurements are indeed available for *Fermi* LGRBs, there is not robust analysis of the completeness or possible biases of this sample.

Regarding the cosmic chemical evolution, more precise determination of chemical abundances as a function of redshift would be very important to constrain galaxy formation models and the LGRB proposed scenarios. More sophisticated numerical simulations are definitely needed to improve the modelisation of the star formation activity and the enrichment of the interstellar medium at different stages of evolution. However, it it is relevant to note that our findings are also in agreement with results by Bignone et al. (2017) who studied the properties of simulated LGRB hosts in the context of the Illustris simulation applying the same LGRB progenitor scenario. And despite the differences between the hydrodinamical simulations used in both works, a consistent metallicity dependence is found.

Finally, our models suggest that chemical effects affect most probably the LGRB rate density, instead of their LF. This result is statistically robust, based on the DIC, and implies a step forward with respect to previous works Wanderman & Piran (2010); Salvaterra et al. (2012); Bignone et al. (2017) Moreover, a clear physical justification exists

for a dependence of the LGRB rate. The lower opacity of low-metallicity stars facilitates a reduced mass loss prior to collapse, and results in the retention of the large amount of angular momentum required to produce LGRBs (Yoon et al., 2006; Woosley & Heger, 2006). No such clear justification exists for a scenario with a metallicity-dependent LF, except for a possible increase in the masses (and hence the Eddington luminosities) of stellar black holes at low metallicities (Crowther et al., 2010).

References

Artale, M. C., Pellizza, L. J., & Tissera, P. B. (2011). Chemical abundances and spatial distribution of long gamma-ray bursts. *MNRAS*, *415*, 3417–3422. URL: http://adsabs.harvard.edu/abs/2011MNRAS.415.3417A. doi:DOI:10.1111/j.1365-2966.2011.18955.x;eprintid:arXiv:1104.5201.

Band, D., Matteson, J., Ford, L., Schaefer, B., Palmer, D., Teegarden, B., Cline, T., Briggs, M., Paciesas, W., Pendleton, G., Fishman, G., Kouveliotou, C., Meegan, C., Wilson, R., & Lestrade, P. (1993). BATSE observations of gamma-ray burst spectra. I - Spectral diversity. *ApJ*, *413*, 281–292. URL: http://adsabs.org/1993ApJ.413.281B. doi:10.1086/172995.

Band, D. L. (2003). Comparison of the Gamma-Ray Burst Sensitivity of Different Detectors. *ApJ*, *588*, 945–951. doi:10.1086/374242. arXiv:astro-ph/0212452.

Behroozi, P. S., Wechsler, R. H., & Conroy, C. (2013). The Average Star Formation Histories of Galaxies in Dark Matter Halos from z = 0-8. *ApJ*, *770*, 57. URL: http://adsabs.org/2013ApJ.770.57B. doi:10.1088/0004-637X/770/1/57.

Belczynski, K., Holz, D. E., Fryer, C. L., Berger, E., Hartmann, D. H., & O'Shea, B. (2010). On the Origin of the Highest Redshift Gamma-Ray Bursts. *ApJ*, *708*, 117–126. doi:10.1088/0004-637X/708/1/117. arXiv:0812.2470.

Bignone, L. A., Tissera, P. B., & Pellizza, L. J. (2017). The metallicity and star formation activity of long gamma-ray burst hosts for z < 3: insights from the Illustris simulation. *MNRAS*, *469*, 4921–4932. doi:10.1093/mnras/stx1132. arXiv:1706.03772.

Buchner, J., Schulze, S., & Bauer, F. E. (2016). Galaxy gas as obscurer: I. GRBs x-ray galaxies and find a N_H ~ M* relation. *ArXiv e-prints*, . arXiv:1610.09379.

Butler, N. R., Kocevski, D., Bloom, J. S., & Curtis, J. L. (2007). A Complete Catalog of Swift Gamma-Ray Burst Spectra and Durations: Demise of a Physical Origin for Pre-Swift High-Energy Correlations. *ApJ*, *671*, 656–677. doi:10.1086/522492. arXiv:0706.1275.

Campisi, M. A., Li, L.-X., & Jakobsson, P. (2010). Redshift distribution and luminosity function of long gamma-ray bursts from cosmological simulations. *MNRAS*, *407*, 1972–1980. URL: http://adsabs.org/2010MNRAS.407.1972C. doi:10.1111/j.1365-2966.2010.17044.x.

Campisi, M. A., Tapparello, C., Salvaterra, R., Mannucci, F., & Colpi, M. (2011). Metallicity properties of the simulated host galaxies of long gamma-ray bursts and the fundamental metallicity relation. *MNRAS*, *417*, 1013–1021. URL: http://mnras.oxfordjournals.org/content/417/2/1013. doi:10.1111/j.1365-2966.2011.19326.x.

Chisari, N. E., Tissera, P. B., & Pellizza, L. J. (2010). Host galaxies of long gamma-ray bursts in the Millennium Simulation. *MNRAS*, *408*, 647–656. URL: http://adsabs.harvard.edu/abs/2010MNRAS.408..647C.

Crowther, P. A., Barnard, R., Carpano, S., Clark, J. S., Dhillon, V. S., & Pollock, A. M. T. (2010). NGC 300 X-1 is a Wolf-Rayet/black hole binary. *MNRAS*, *403*, L41–L45. doi:10.1111/j.1745-3933.2010.00811.x. arXiv:1001.4616.

Dai, X. (2009). Intensity Distribution and Luminosity Function of the Swift Gamma-Ray Bursts. *ApJl*, *697*, L68–L71. doi:10.1088/0004-637X/697/1/L68. arXiv:0812.4466.

Daigne, F., Rossi, E. M., & Mochkovitch, R. (2006). The redshift distribution of Swift gamma-ray bursts: evidence for evolution. *MNRAS*, *372*, 1034–1042. URL: http://adsabs.org/2006MNRAS.372.1034D. doi:10.1111/j.1365-2966.2006.10837.x.

De Lucia, G., & Blaizot, J. (2007). The hierarchical formation of the brightest cluster galaxies. *MNRAS*, *375*, 2–14. doi:10.1111/j.1365-2966.2006.11287.x. arXiv:astro-ph/0606519.

De Rossi, M. E., Avila-Reese, V., Tissera, P. B., González-Samaniego, A., & Pedrosa, S. E. (2013). On the mass assembly of low-mass galaxies in hydrodynamical simulations of structure formation. *MNRAS*, *435*, 2736–2752. doi:10.1093/mnras/stt1486. arXiv:1308.2727.

Della Valle, M., Malesani, D., Bloom, J. S., Benetti, S., Chincarini, G., D'Avanzo, P., Foley, R. J., Covino, S., Melandri, A., Piranomonte, S., Tagliaferri, G., Stella, L., Gilmozzi, R., Antonelli, L. A., Campana, S., Chen, H.-W., Filliatre, P., Fiore, F., Fugazza, D., Gehrels, N., Hurley, K., Mirabel, I. F., Pellizza, L. J., Piro, L., & Prochaska, J. X. (2006). Hypernova Signatures in the Late Rebrightening of GRB 050525A. *ApJl*, *642*, L103–L106. doi:10.1086/504636. arXiv:astro-ph/0604109.

Elliott, J., Greiner, J., Khochfar, S., Schady, P., Johnson, J. L., & Rau, A. (2012). The long γ-ray burst rate and the correlation with host galaxy properties. *A&A*, *539*, A113. doi:10.1051/0004-6361/201118561. arXiv:1202.1225.

Firmani, C., Avila-Reese, V., Ghisellini, G., & Tutukov, A. V. (2004). Formation Rate, Evolving Luminosity Function, Jet Structure, and Progenitors for Long Gamma-Ray Bursts. *ApJ*, *611*, 1033–1040. URL: http://adsabs.org/2004ApJ.611.1033F. doi:10.1086/422186.

Ghirlanda, G., Nava, L., Ghisellini, G., & Firmani, C. (2007). Confirming the γ-ray burst spectral-energy correlations in the era of multiple time breaks. *A&A*, *466*, 127–136. doi:10.1051/0004-6361:20077119. arXiv:astro-ph/0702352.

Graham, J. F., & Fruchter, A. S. (2013). The Metal Aversion of Long-duration Gamma-Ray Bursts. *ApJ*, *774*, 119. URL: http://adsabs.harvard.edu/abs/2013ApJ...774..119G. doi:10.1088/0004-637X/774/2/119.

Graham, J. F., Fruchter, A. S., Levesque, E. M., Kewley, L. J., Tanvir, N. R., Levan, A. J., Patel, S. K., Misra, K., Huang, K.-H., Reichart, D. E., Nysewander, M., & Schady, P. (2015). High Metallicity LGRB Hosts. *ArXiv e-prints*, . arXiv:1511.00667.

Gruber, D., Goldstein, A., Weller von Ahlefeld, V., Narayana Bhat, P., Bissaldi, E., Briggs, M. S., Byrne, D., Cleveland, W. H., Connaughton, V., Diehl, R., Fishman, G. J., Fitzpatrick, G., Foley, S., Gibby, M., Giles, M. M., Greiner, J., Guiriec, S., van der Horst, A. J., von Kienlin, A., Kouveliotou, C., Layden, E., Lin, L., Meegan, C. A., McGlynn, S., Paciesas, W. S., Pelassa, V., Preece, R. D., Rau, A., Wilson-Hodge, C. A., Xiong, S., Younes, G., & Yu, H.-F. (2014). The Fermi GBM Gamma-Ray Burst Spectral Catalog: Four Years of Data. *ApJS*, *211*, 12. URL: http://adsabs.org/2014ApJS.211.12G. doi:10.1088/0067-0049/211/1/12.

Hjorth, J., Malesani, D., Jakobsson, P., Jaunsen, A. O., Fynbo, J. P. U., Gorosabel, J., Krühler, T., Levan, A. J., Michałowski, M. J., Milvang-Jensen, B., Møller, P., Schulze, S., Tanvir, N. R.,

& Watson, D. (2012). The Optically Unbiased Gamma-Ray Burst Host (TOUGH) Survey. I. Survey Design and Catalogs. *ApJ*, *756*, 187. URL: http://adsabs.harvard.edu/abs/2012ApJ. .756..187H. doi:10.1088/0004-637X/756/2/187.

Hjorth, J., Sollerman, J., Møller, P., Fynbo, J. P. U., Woosley, S. E., Kouveliotou, C., Tanvir, N. R., Greiner, J., Andersen, M. I., Castro-Tirado, A. J., Castro Cerón, J. M., Fruchter, A. S., Gorosabel, J., Jakobsson, P., Kaper, L., Klose, S., Masetti, N., Pedersen, H., Pedersen, K., Pian, E., Palazzi, E., Rhoads, J. E., Rol, E., van den Heuvel, E. P. J., Vreeswijk, P. M., Watson, D., & Wijers, R. A. M. J. (2003). A very energetic supernova associated with the γ-ray burst of 29 March 2003. *Nature*, *423*, 847–850. URL: http://adsabs.org/2003Natur.423.847H. doi:10.1038/nature01750.

Howell, E. J., Coward, D. M., Stratta, G., Gendre, B., & Zhou, H. (2014). Constraining the rate and luminosity function of Swift gamma-ray bursts. *MNRAS*, *444*, 15–28. doi:10.1093/mnras/stu1403. arXiv:1407.2333.

Iwamoto, K., Brachwitz, F., Nomoto, K., Kishimoto, N., Umeda, H., Hix, W. R., & Thielemann, F.-K. (1999). Nucleosynthesis in Chandrasekhar Mass Models for Type IA Supernovae and Constraints on Progenitor Systems and Burning-Front Propagation. *ApJS*, *125*, 439–462. URL: http://adsabs.org/1999ApJS.125.439I. doi:10.1086/313278.

Jakobsson, P., Hjorth, J., Fynbo, J. P. U., Watson, D., Pedersen, K., Björnsson, G., & Gorosabel, J. (2004). Swift Identification of Dark Gamma-Ray Bursts. *ApJl*, *617*, L21–L24. doi:10.1086/427089. arXiv:astro-ph/0411036.

Japelj, J., Vergani, S. D., Salvaterra, R., D'Avanzo, P., Mannucci, F., Fernandez-Soto, A., Boissier, S., Hunt, L. K., Atek, H., Rodríguez-Muñoz, L., Scodeggio, M., Cristiani, S., Le Floc'h, E., Flores, H., Gallego, J., Ghirlanda, G., Gomboc, A., Hammer, F., Perley, D. A., Pescalli, A., Petitjean, P., Puech, M., Rafelski, M., & Tagliaferri, G. (2016). Are long gamma-ray bursts biased tracers of star formation? Clues from the host galaxies of the Swift/BAT6 complete sample of bright LGRBs. II. Star formation rates and metallicities at $z < 1$. *A&A*, *590*, A129. doi:10.1051/0004-6361/201628314. arXiv:1604.01034.

Jiménez, N., Tissera, P. B., & Matteucci, F. (2015). Type Ia Supernova Progenitors and Chemical Enrichment in Hydrodynamical Simulations. I. The Single-degenerate Scenario. *ApJ*, *810*, 137. doi:10.1088/0004-637X/810/2/137. arXiv:1402.4137.

Jimenez, R., & Piran, T. (2013). Reconciling the Gamma-Ray Burst Rate and Star Formation Histories. *ApJ*, *773*, 126. URL: http://adsabs.harvard.edu/abs/2013ApJ...773..126J. doi:10.1088/0004-637X/773/2/126.

Kaneko, Y., Preece, R. D., Briggs, M. S., Paciesas, W. S., Meegan, C. A., & Band, D. L. (2006). The Complete Spectral Catalog of Bright BATSE Gamma-Ray Bursts. *ApJS*, *166*, 298–340. URL: http://adsabs.org/2006ApJS.166.298K. doi:10.1086/505911.

Kewley, L. J., & Dopita, M. A. (2002). Using Strong Lines to Estimate Abundances in Extragalactic H II Regions and Starburst Galaxies. *ApJs*, *142*, 35–52. doi:10.1086/341326. arXiv:astro-ph/0206495.

von Kienlin, A., Meegan, C. A., Paciesas, W. S., Bhat, P. N., Bissaldi, E., Briggs, M. S., Burgess, J. M., Byrne, D., Chaplin, V., Cleveland, W., Connaughton, V., Collazzi, A. C., Fitzpatrick, G., Foley, S., Gibby, M., Giles, M., Goldstein, A., Greiner, J., Gruber, D., Guiriec, S., van der Horst, A. J., Kouveliotou, C., Layden, E., McBreen, S., McGlynn, S., Pelassa, V., Preece, R. D., Rau, A., Tierney, D., Wilson-Hodge, C. A., Xiong, S., Younes, G., & Yu, H.-F. (2014). The Second Fermi GBM Gamma-Ray Burst Catalog: The First Four Years. *ApJS*, *211*, 13. URL: http://adsabs.org/2014ApJS.211.13V. doi:10.1088/0067-0049/211/1/13.

Langer, N., & Norman, C. A. (2006). On the Collapsar Model of Long Gamma-Ray Bursts:Constraints from Cosmic Metallicity Evolution. *ApJ Letters*, *638*, L63–L66. URL: http://adsabs.org/2006ApJ.638L.63L. doi:10.1086/500363.

Le Floc'h, E., Duc, P.-A., Mirabel, I. F., Sanders, D. B., Bosch, G., Diaz, R. J., Donzelli, C. J., Rodrigues, I., Courvoisier, T. J.-L., Greiner, J., Mereghetti, S., Melnick, J., Maza, J., & Minniti, D. (2003). Are the hosts of gamma-ray bursts sub-luminous and blue galaxies? *A&A*, *400*, 499–510. URL: http://adsabs.harvard.edu/abs/2003A%26A...400..499L. doi:10.1051/0004-6361:20030001.

Levesque, E. M., Kewley, L. J., Graham, J. F., & Fruchter, A. S. (2010). A High-metallicity Host Environment for the Long-duration GRB 020819. *ApJ Letters*, *712*, L26–L30. URL: http://adsabs.harvard.edu/abs/2010ApJ...712L..26L. doi:10.1088/2041-8205/712/1/L26.

Liddle, A. R. (2007). Information criteria for astrophysical model selection. *MNRAS*, *377*, L74–L78. URL: http://adsabs.org/2007MNRAS.377L.74L. doi:10.1111/j.1745-3933.2007.00306.x.

Maiolino, R., Nagao, T., Grazian, A., Cocchia, F., Marconi, A., Mannucci, F., Cimatti, A., Pipino, A., Ballero, S., Calura, F., Chiappini, C., Fontana, A., Granato, G. L., Matteucci, F., Pastorini, G., Pentericci, L., Risaliti, G., Salvati, M., & Silva, L. (2008). AMAZE. I. The evolution of the mass-metallicity relation at z > 3. *A&A*, *488*, 463–479. URL: http://adsabs.harvard.edu/abs/2008A%26A...488..463M. doi:10.1051/0004-6361:200809678.

Mosconi, M. B., Tissera, P. B., Lambas, D. G., & Cora, S. A. (2001). Chemical evolution using smooth particle hydrodynamical cosmological simulations - I. Implementation, tests and first results. *MNRAS*, *325*, 34–48. URL: http://adsabs.org/2001MNRAS.325.34M. doi:10.1046/j.1365-8711.2001.04198.x.

Nava, L., Ghirlanda, G., Ghisellini, G., & Firmani, C. (2008). Peak energy of the prompt emission of long gamma-ray bursts versus their fluence and peak flux. *MNRAS*, *391*, 639–652. URL: http://adsabs.org/2008MNRAS.391.639N. doi:10.1111/j.1365-2966.2008.13758.x.

Nuza, S. E., Tissera, P. B., Pellizza, L. J., Lambas, D. G., Scannapieco, C., & de Rossi, M. E. (2007). The host galaxies of long-duration gamma-ray bursts in a cosmological hierarchical scenario. *MNRAS*, *375*, 665–672. URL: http://adsabs.harvard.edu/abs/2007MNRAS.375..665N. doi:DOI:10.1111/j.1365-2966.2006.11324.x;eprintid:arXiv:astro-ph/0611122.

Paciesas, W. S., Meegan, C. A., von Kienlin, A., Bhat, P. N., Bissaldi, E., Briggs, M. S., Burgess, J. M., Chaplin, V., Connaughton, V., Diehl, R., Fishman, G. J., Fitzpatrick, G., Foley, S., Gibby, M., Giles, M., Goldstein, A., Greiner, J., Gruber, D., Guiriec, S., van der Horst, A. J., Kippen, R. M., Kouveliotou, C., Lichti, G., Lin, L., McBreen, S., Preece, R. D., Rau, A., Tierney, D., & Wilson-Hodge, C. (2012). The Fermi GBM Gamma-Ray Burst Catalog: The First Two Years. *ApJS*, *199*, 18. doi:10.1088/0067-0049/199/1/18. arXiv:1201.3099.

Pedrosa, S. E., & Tissera, P. B. (2015). Angular momentum evolution for galaxies in a Λ-CDM scenario. *A&A*, *584*, A43. doi:10.1051/0004-6361/201526440. arXiv:1508.07220.

Perley, D. A., Cenko, S. B., Bloom, J. S., Chen, H.-W., Butler, N. R., Kocevski, D., Prochaska, J. X., Brodwin, M., Glazebrook, K., Kasliwal, M. M., Kulkarni, S. R., Lopez, S., Ofek, E. O., Pettini, M., Soderberg, A. M., & Starr, D. (2009). The Host Galaxies of Swift Dark Gamma-ray Bursts: Observational Constraints on Highly Obscured and Very High Redshift GRBs. *AJ*, *138*, 1690–1708. doi:10.1088/0004-6256/138/6/1690. arXiv:0905.0001.

Perley, D. A., Krühler, T., Schulze, S., de Ugarte Postigo, A., Hjorth, J., Berger, E., Cenko, S. B., Chary, R., Cucchiara, A., Ellis, R., Fong, W., Fynbo, J. P. U., Gorosabel, J., Greiner, J., Jakobsson, P., Kim, S., Laskar, T., Levan, A. J., Michałowski, M. J., Milvang-Jensen, B., Tanvir, N. R., Thöne, C. C., & Wiersema, K. (2016). The Swift Gamma-Ray Burst Host Galaxy Legacy Survey. I. Sample Selection and Redshift Distribution. *ApJ*, *817*, 7. doi:10.3847/0004-637X/817/1/7. arXiv:1504.02482.

Perley, D. A., Levan, A. J., Tanvir, N. R., Cenko, S. B., Bloom, J. S., Hjorth, J., Krühler, T., Filippenko, A. V., Fruchter, A., Fynbo, J. P. U., Jakobsson, P., Kalirai, J., Milvang-Jensen, B., Morgan, A. N., Prochaska, J. X., & Silverman, J. M. (2013). A Population of Massive, Luminous Galaxies Hosting Heavily Dust-obscured Gamma-Ray Bursts: Implications for the Use of GRBs as Tracers of Cosmic Star Formation. *ApJ*, *778*, 128. URL: http://adsabs.harvard.edu/abs/2013ApJ...778..128P. doi:10.1088/0004-637X/778/2/128.

Salpeter, E. E. (1955). The Luminosity Function and Stellar Evolu-

tion. *ApJ*, *121*, 161. doi:`10.1086/145971`.

Salvaterra, R., Campana, S., Vergani, S. D., Covino, S., D'Avanzo, P., Fugazza, D., Ghirlanda, G., Ghisellini, G., Melandri, A., Nava, L., Sbarufatti, B., Flores, H., Piranomonte, S., & Tagliaferri, G. (2012). A Complete Sample of Bright Swift Long Gamma-Ray Bursts. I. Sample Presentation, Luminosity Function and Evolution. *ApJ*, *749*, 68. URL: `http://adsabs.org/2012ApJ.749.68S`. doi:`10.1088/0004-637X/749/1/68`.

Salvaterra, R., & Chincarini, G. (2007). The Gamma-Ray Burst Luminosity Function in the Light of the Swift 2 Year Data. *ApJ Letters*, *656*, L49–L52. URL: `http://adsabs.org/2007ApJ.656L.49S`. doi:`10.1086/512606`.

Salvaterra, R., Guidorzi, C., Campana, S., Chincarini, G., & Tagliaferri, G. (2009). Evidence for luminosity evolution of long gamma-ray bursts in Swift data. *MNRAS*, *396*, 299–303. doi:`10.1111/j.1365-2966.2008.14343.x`. `arXiv:0805.4104`.

Savaglio, S., Glazebrook, K., & Le Borgne, D. (2009). The Galaxy Population Hosting Gamma-Ray Bursts. *ApJ*, *691*, 182–211. URL: `http://adsabs.harvard.edu/abs/2009ApJ..691..182S`. doi:`10.1088/0004-637X/691/1/182`.

Savaglio, S., Rau, A., Greiner, J., Krühler, T., McBreen, S., Hartmann, D. H., Updike, A. C., Filgas, R., Klose, S., Afonso, P., Clemens, C., Küpcü Yoldas, A., Olivares E., F., Sudilovsky, V., & Szokoly, G. (2012). Supersolar metal abundances in two galaxies at z ˜ 3.57 revealed by the GRB 090323 afterglow spectrum. *MNRAS*, *420*, 627–636. URL: `http://adsabs.harvard.edu/abs/2012MNRAS.420..627S`. doi:`10.1111/j.1365-2966.2011.20074.x`.

Scannapieco, C., Tissera, P. B., White, S. D. M., & Springel, V. (2005). Feedback and metal enrichment in cosmological smoothed particle hydrodynamics simulations - I. A model for chemical enrichment. *MNRAS*, *364*, 552–564. URL: `http://adsabs.org/2005MNRAS.364.552S`. doi:`10.1111/j.1365-2966.2005.09574.x`.

Scannapieco, C., Tissera, P. B., White, S. D. M., & Springel, V. (2006). Feedback and metal enrichment in cosmological SPH simulations - II. A multiphase model with supernova energy feedback. *MNRAS*, *371*, 1125–1139. URL: `http://adsabs.org/2006MNRAS.371.1125S`. doi:`10.1111/j.1365-2966.2006.10785.x`.

Springel, V. (2005). The cosmological simulation code GADGET-2. *MNRAS*, *364*, 1105–1134. URL: `http://adsabs.harvard.edu/abs/2005MNRAS.364.1105S`.

Springel, V., White, S. D. M., Jenkins, A., Frenk, C. S., Yoshida, N., Gao, L., Navarro, J., Thacker, R., Croton, D., Helly, J., Peacock, J. A., Cole, S., Thomas, P., Couchman, H., Evrard, A., Colberg, J., & Pearce, F. (2005). Simulations of the formation, evolution and clustering of galaxies and quasars. *Nature*, *435*, 629–636. doi:`10.1038/nature03597`. `arXiv:astro-ph/0504097`.

Stanek, K. Z., Gnedin, O. Y., Beacom, J. F., Gould, A. P., Johnson, J. A., Kollmeier, J. A., Modjaz, M., Pinsonneault, M. H., Pogge, R., & Weinberg, D. H. (2006). Protecting Life in the Milky Way: Metals Keep the GRBs Away. *Acta Astronomica*, *56*, 333–345. URL: `http://adsabs.org/2006AcA.56.333S`.

Stern, B. E., Tikhomirova, Y., Kompaneets, D., Svensson, R., & Poutanen, J. (2001). An Off-Line Scan of the BATSE Daily Records and a Large Uniform Sample of Gamma-Ray Bursts. *ApJ*, *563*, 80–94. URL: `http://adsabs.org/2001ApJ.563.80S`. doi:`10.1086/322295`.

Tan, W.-W., & Wang, F. Y. (2015). Research on the redshift evolution of luminosity function and selection effect of GRBs. *MNRAS*, *454*, 1785–1791. doi:`10.1093/mnras/stv2007`. `arXiv:1508.07094`.

Tissera, P. B., Pedrosa, S. E., Sillero, E., & Vilchez, J. M. (2016). The gas metallicity gradient and the star formation activity of disc galaxies. *MNRAS*, *456*, 2982–2992. doi:`10.1093/mnras/stv2736`. `arXiv:1511.08227`.

Tremonti, C. A., Heckman, T. M., Kauffmann, G., Brinchmann, J., Charlot, S., White, S. D. M., Seibert, M., Peng, E. W., Schlegel, D. J., Uomoto, A., Fukugita, M., & Brinkmann, J. (2004). The Origin of the Mass-Metallicity Relation: Insights from 53,000 Star-forming Galaxies in the Sloan Digital Sky Survey. *ApJ*, *613*, 898–913. URL: `http://adsabs.harvard.edu/abs/2004ApJ..613..898T`. doi:`10.1086/423264`.

Vedrenne, G., & Atteia, J.-L. (2009). *Gamma-Ray Bursts*. Springer-Verlag. doi:`10.1007/978-3-540-39088-6`.

Vergani, S. D., Salvaterra, R., Japelj, J., Le Floc'h, E., D'Avanzo, P., Fernandez-Soto, A., Krühler, T., Melandri, A., Boissier, S., Covino, S., Puech, M., Greiner, J., Hunt, L. K., Perley, D., Petitjean, P., Vinci, T., Hammer, F., Levan, A., Mannucci, F., Campana, S., Flores, H., Gomboc, A., & Tagliaferri, G. (2015). Are long gamma-ray bursts biased tracers of star formation? Clues from the host galaxies of the Swift/BAT6 complete sample of LGRBs . I. Stellar mass at z < 1. *A&A*, *581*, A102. doi:`10.1051/0004-6361/201425013`. `arXiv:1409.7064`.

Wanderman, D., & Piran, T. (2010). The luminosity function and the rate of Swift's gamma-ray bursts. *MNRAS*, *406*, 1944–1958. URL: `http://adsabs.harvard.edu/abs/2010MNRAS.406.1944W`. doi:`10.1111/j.1365-2966.2010.16787.x`.

Wijers, R. A. M. J., Bloom, J. S., Bagla, J. S., & Natarajan, P. (1998). Gamma-ray bursts from stellar remnants - Probing the universe at high redshift. *MNRAS*, *294*, L13–L17. URL: `http://adsabs.harvard.edu/abs/1998MNRAS.294L..13W`. doi:`10.1046/j.1365-8711.1998.01328.x`.

Woosley, S. E. (1993). Gamma-ray bursts from stellar mass accretion disks around black holes. *ApJ*, *405*, 273–277. URL: `http://adsabs.harvard.edu/abs/1993ApJ...405..273W`. doi:`10.1086/172359`.

Woosley, S. E., & Heger, A. (2006). The Progenitor Stars of Gamma-Ray Bursts. *ApJ*, *637*, 914–921. URL: `http://adsabs.harvard.edu/abs/2006ApJ...637..914W`. doi:`10.1086/498500`.

Woosley, S. E., & Weaver, T. A. (1995). The Evolution and Explosion of Massive Stars. II. Explosive Hydrodynamics and Nucleosynthesis. *ApJS*, *101*, 181. URL: `http://adsabs.org/1995ApJS.101.181W`. doi:`10.1086/192237`.

Yonetoku, D., Murakami, T., Nakamura, T., Yamazaki, R., Inoue, A. K., & Ioka, K. (2004). Gamma-Ray Burst Formation Rate Inferred from the Spectral Peak Energy-Peak Luminosity Relation. *ApJ*, *609*, 935–951. URL: `http://adsabs.org/2004ApJ.609.935Y`. doi:`10.1086/421285`.

Yoon, S.-C., Langer, N., & Norman, C. (2006). Single star progenitors of long gamma-ray bursts. I. Model grids and redshift dependent GRB rate. *A&A*, *460*, 199–208. URL: `http://adsabs.harvard.edu/abs/2006A%26A...460..199Y`. doi:`10.1051/0004-6361:20065912`.